Research Square

Preprints are preliminary reports that have not undergone peer review.
They should not be considered conclusive, used to inform clinical practice,
or referenced by the media as validated information.

The number of clasts as quantity governing the mobility of rock avalanches

Bruno Cagnoli

bruno.cagnoli@ingv.it

Istituto Nazionale di Geofisica e Vulcanologia https://orcid.org/0000-0003-3263-5345

Research Article

Keywords: Rock avalanches, Energy apportionment, Energy dissipation, Clast number, Flow volume, Mobility

Posted Date: August 6th, 2026

DOI: https://doi.org/10.21203/rs.3.rs-10597740/v1

License: This work is licensed under a Creative Commons Attribution 4.0 International License.
Read Full License

Additional Declarations: The authors declare no competing interests.

The number of clasts as quantity governing the mobility of rock avalanches

Bruno Cagnoli

Istituto Nazionale di Geofisica e Vulcanologia (INGV), Viale Carlo Berti Pichat 6/2, 40127 Bologna, Italy

Email: bruno.cagnoli@ingv.it

**corresponding author*

Abstract

Rock avalanches are extremely hazardous flows of rock fragments causing destruction in mountainous areas worldwide. The physics controlling their behavior is however hotly debated. Here, numerical simulations and field data indicate that the number of clasts of a flow is the all-important quantity governing its mobility. Indeed, the mobility increase caused by a flow volume increase and that caused by a grain size decrease (all else being equal) are produced by a feature they share: an increase in number of clasts. Notably, the ratio of flow volume to the volume of a medium grain size is a proxy for the unknowable number of clasts of natural avalanches. Here, data demonstrate that, in these flows, the decrease of the work done by the non-conservative forces (per unit of potential energy drop) is a property intrinsic to a volume increase or a grain size decrease where more energy is allocated to downslope translational motion (per unit of dissipated energy) and less energy is diverted into clast agitational and rotational motion (per unit of flow mass). This energy apportionment mechanism affects mobility of volumes ranging from significantly less than 0.5 million m^3 to many million m^3. Mobility predictions are required for risk assessment of rock avalanches in populated areas.

Keywords Rock avalanches, Energy apportionment, Energy dissipation, Clast number, Flow volume, Mobility

Introduction

Here, the focus is on dense flows of angular rock fragments that are dry, unsteady, nonuniform, able to dilate vertically and with possible lateral confinement such as rock avalanches [1]. Their exceptional destructive power results from their large momentum [2–7]. One of the most important geoscientific conundrums to unravel is that of the physics determining their well-known positive correlation between volume and mobility. This correlation has baffled scientists ever since the impressive large runouts of the biggest flows were first discovered [8–15]. Volume thresholds (such as 0.5 or 5 million m^3) were introduced while invoking a special mobility mechanism specific for larger volumes [16–19]. In fact, in the field, as importantly illustrated by Corominas [20], the reduction of landslide mobility as volume decreases is continuous from approximately 10^{10} to 10 m^3, and, as such, compatible with a single mechanism acting in this entire volume spectrum. Indeed, 3D DEM simulations [21,22] demonstrated that this volume effect occurs also with volumes as small as 4000–14500 m^3, provided that the flows are dense and travel on a rough subsurface in wide channels. This effect, however, is the opposite of that shown by the centers of mass (but not by the fronts [22,23]) of laboratory miniature flows [23] which underestimate the stresses of large-scale flows [21,24]. The larger-scale flows of the simulations in refs. [21,22] are those whose energy dissipation mechanism is analyzed here to explain the mobility-volume relationship of rock avalanches. The aim of this paper is to assess the effect of the number of clasts on rock avalanche mobility. Simulation results are validated by comparison with field data.

Method: introduction

Three-dimensional numerical simulations

The three-dimensional numerical simulations of granular flows of angular rock fragments studied here are Discrete Element Method (i.e., DEM [25]) models. In refs. [21,22], the computational

avalanches have different geometric scales according to a factor n equal to either 1, 100 or 1000 ($n = 1$ refers to laboratory miniature flows). The five largest-scale flows (with $n = 1000$) are those examined here when in wide channels and on a rough subsurface. The contact model of these DEM simulations is illustrated by ref. [26].

These granular flows differ only in volume or grain size (Table 1). Each monodisperse flow has cubic particles (2700 kg/m^3 in density) with the same grain size that is either 0.5, 1 or 2 m. Flow volume ranges from ~4080 to ~14533 m^3. These features result in flows which, when with maximum speed, vary from 441 to 509 m in length. The number of clasts of these avalanches is shown in Table 1. These flows descend a 3D channel (Fig. 1) that has a longitudinal profile with an initial short straight incline and, then, a curved portion whose equation [21,22] is similar to that of Mt Mayon profile [27]. The channel has a trapezoidal transversal cross-section whose lateral-side inclination θ is equal to $27°$ in all simulations (flow mobility is also a function of this lateral-side inclination [28]). Channel width w is measured as the shortest basal distance between the inclined sidewalls and it is equal to either 6 or 26 m. There are no intergranular fluids (such as gases or water).

No gate [29] is used to release the granular material from rest at the top of the slope so that the system is free from unnecessary frictional forces. The initial polyhedral granular masses, instead, collapse under the influence of gravity and, after an initial deformation, they flow and acquire a fully developed shape of travel, first, accelerating downslope and reaching a maximum speed and, then, decelerating before forming a final deposit. The deposited granular material consists always of two portions: 1) a more proximal heap that is much more elongated than thick (the deposit proper) and 2) a more distal distribution of isolated clasts.

Mobility parameters

These computational flows of angular rock fragments travelling on a rough subsurface in wide channels are characterized by different values of the dimensionless granular scaling parameter [21,22]

$$\psi = \frac{\delta^2}{V^{1/3} w}, \tag{1}$$

where δ is the grain size, w is the channel width and V is the flow volume computed as the volume of the solid mass (Figs. 2a, b). In flows that are not significantly channelized (as with field data in Figs. 2c, d), ψ is replaced by

$$\psi' = \frac{\delta^3}{V}. \tag{2}$$

Two mobility parameters are considered: one for the flow fronts (μ_H) and one for the center of mass (μ_A). Functional relationships between these mobility parameters and ψ, exactly or approximately, hold [21,22] for dense flows on a rough subsurface in wide channels (Figs. 2a, b).

Given the complexity of flow front dynamics due to the decrease of the solid volume fraction from the flow interior outwards [30], the concept of the front of a portion of flow (inside the flow) was introduced [22] where this portion is a volume percent ($vol\%$) measured from the flow rear end (where $vol\% = 0$). The values of $vol\%$ considered were 80, 85, 90, 95 and 99. In the simulations, the Heim's coefficient (i.e., the reciprocal of flow front mobility) is therefore computed for the front of each $vol\%$ as

$$\mu_H = \frac{h_{Hvol\%}}{l_{Hvol\%}}, \quad (3)$$

where $h_{Hvol\%}$ and $l_{Hvol\%}$ are the distances, in the vertical and horizontal direction respectively, between the rear top end of the granular mass before release (i.e., of the slope scarp in nature) and the front of that $vol\%$ of deposit (Fig. 2).

The fronts of $80 \leq vol\% \leq 95$ with the behavior of the dense granular regime are those whose data points are best-fitted by straight lines in Fig. 2a. Their flows have also more distal fronts (such as those of $vol\% = 99$) that are not best-fitted by these straight lines because they are significantly affected by clast saltation [22]. Thus, different fronts of a single granular flow can behave differently. However, with rock avalanches in nature, the overall mass of the distal distribution of isolated clasts (which has a disperse regime behavior and where the front of $vol\% \geq 99$ is expected) is much smaller (and more difficult to spot in the field) than that of the rest of the flow with a dense regime behavior. In this case, flow front mobility measured in the field (as in Fig. 2c) can be assumed to be that of the deposit proper.

Regarding the mobility of the centre of mass of the computational flows (Fig. 1), its reciprocal is

$$\mu_A = \frac{h_A}{l_A}, \quad (4)$$

where h_A is the vertical drop of the centre of mass of all granular material (i.e., deposit proper plus distal distribution together) and l_A is its horizontal distance of travel (Fig. 2b). With rock avalanches of the dense regime in nature, μ_A measured in the field (as in Fig. 2d) can also be assumed (like μ_H) to be that of the deposit proper.

Method: energy analysis

Energy apportionment and dissipation parameters

Here, the mobility behaviors of the computational flows (Figs. 2a, b) are explained by quantifying the apportionment of energy among its different forms during the entire flow history. Since this energy analysis is new, the following parameters are introduced for the first time.

In all computational flows, data point index i starts out as 0 for the granular mass before release so that $i \geq 0$. Quantity ℓ_i represents the slope position of the flow center of mass as the distance between the projection of the center of mass on the slope before the gravitational collapse ($i = 0$) and its projection at time $t_i = i \cdot \Delta t$. Time step Δt is equal to 0.2 sec in all simulations. Index j is that of the displacement interval $\Delta\ell_j$ on the slope between positions ℓ_{i-1} and ℓ_i where $i = j$ (so that $j \geq 1$). The length of $\Delta\ell_j$ varies because flows accelerate and decelerate whereas Δt is constant.

Any position ℓ_i of the center of mass is characterized by the absolute value of the work done on the flow by the non-conservative forces to travel from ℓ_0 to ℓ_i:

$$\sum_{1}^{j=i} \left| W_j^{NC} \right|, \tag{5}$$

which is the irreversible energy loss due to clast interactions with the subsurface and among themselves inside the flow. In expression (5), the non-conservative work in each slope interval $\Delta\ell_j$ is

$$W_j^{NC} = TKE_p + RKE_p + PE_p - TKE_{p-1} - RKE_{p-1} - PE_{p-1}, \tag{6}$$

153 whose translational kinetic energy TKE, rotational kinetic energy RKE and gravitational potential
154 energy PE are the total ones of the flows in positions ℓ_{p-1} and ℓ_p where $p = j$. "Total" means that
155 each of those energy forms is the sum of the contributions of each and all clasts (i.e., of total flow
156 mass M_{tot}). Any position ℓ_i is characterized also by a drop in gravitational potential energy $PE_0 -$
157 PE_i (where PE_0 is the initial potential energy of the granular mass before release). Therefore,
158 dimensionless parameter
159
160 $$\widehat{W}_i^{NC} = \frac{\sum_1^{j=i} \left| W_j^{NC} \right|}{PE_0 - PE_i} \quad (7)$$
161
162 represents the magnitude of the work done by the non-conservative forces per unit of potential energy
163 drop to travel from ℓ_0 to ℓ_i. This parameter is plotted versus normalized distance ℓ_i/ℓ_{max}, where
164 ℓ_{max} is the final travel distance of the center of mass of the most mobile flow among the two (Fig.
165 3a) or three (Fig. 5a) that are compared in the graph. The resulting curves allow energies dissipated
166 by different flows to be compared when their centers of mass have the same position on the slope.
167 Insets in Figs. 3a and 5a include the initial gravitational collapses, whose relatively large initial values
168 of $\left| W_j^{NC} \right|$ quickly decrease in relation to $PE_0 - PE_i$ as i increases in the summation of Eq. (7).
169 Needless to say, the initial gravitational collapses shape the early portions of all curves in all graphs.
170
171 In each position ℓ_i, quantity
172
173 $$\Delta TKE_i = TKE_i - TKE_i^G \quad (8)$$
174
175 is an increasing function of clast agitation because it is that portion of TKE_i (the translational kinetic
176 energy in all directions of all clasts) that belongs to the granular system in addition to the translational
177 kinetic energy TKE_i^G in the downslope direction of M_{tot} (i.e., of the center of mass). Since flow speed

178 also affects clast agitation, it is the ΔTKE_i per unit of downslope translational kinetic energy that is
179 considered so that the dimensionless parameter adopted here is
180
181 $$\Lambda_i = \frac{TKE_i^G}{\Delta TKE_i}. \quad (9)$$
182
183 Thus, parameter Λ_i is the reciprocal of an increasing function of clast agitation plotted, in Fig. 4,
184 versus ℓ_i/ℓ_{max}. Its initial values are very large because the entire mass is mainly translating during
185 the initial gravitational collapse (insets in Fig. 4). Its final values are very small because of the only
186 agitated clasts of the small portion of the total mass that is still moving at the end (Fig. 4). The
187 reciprocal of Λ_i increases as flow volume decreases or as grain size increases (all else being equal)
188 in agreement with other parameters used to assess clast agitation [21,26].
189
190 Since work W_j^{NC} is a function of the length of its displacement $\Delta\ell_j$, for each slope interval $\Delta\ell_j$, it
191 is defined quantity ω_j^{NC} as the magnitude of the work done by the non-conservative forces (at the
192 base and inside the flow) in a unit of travel distance. This enables the calculation, for each slope
193 interval $\Delta\ell_j$, of
194
195 $$T_j^{\omega} = \frac{\overline{TKE^G}_j}{\omega_j^{NC}}, \quad (10)$$
196
197 which is the dimensionless ratio of the average downslope translational kinetic energy of the center
198 of mass to the magnitude of the non-conservative work in a unit of travel distance. For each slope
199 interval $\Delta\ell_j$, the average clast rotational kinetic energy per unit of flow mass is
200

$$R_j^M = \frac{\overline{RKE_j}}{M_{tot}}. \quad (11)$$

In Eqs. (10) and (11), the averages are those of the values at the two ends of $\Delta\ell_j$.

In Figs. 3 and 5, T_j^ω and R_j^M are plotted versus the travel history parameter

$$\Phi_j = \frac{\overline{TKE^G}_j}{\overline{TKE^G}_{max}}, \quad (12)$$

whose value 1) increases from 0 as the flow accelerates downslope after the initial gravitational slope collapse, 2) becomes equal to 1 when the maximum value $\overline{TKE^G}_{max}$ of the average translational kinetic energy of the center of mass is reached and 3) decreases as the flow decelerates before the final deposition when it is 0 again. Each value of Φ_j identifies the period of time when its correspondent $\Delta\ell_j$ distance is travelled. In graphs of T_j^ω or R_j^M, their values of different flows are juxtaposed for comparison in the same travel history period Φ_j.

Results and Discussion

Number of clasts and mobility in numerical simulations

This section illustrates the mobility results of numerical simulations obtained, in terms of μ_A and μ_H, by refs. [21,22]. These DEM simulations demonstrate that volume is not the only quantity affecting mobility because, in the dense granular regime on a rough subsurface in wide channels, μ_A and μ_H are functions of $\psi = \delta^2/(V^{1/3}w)$. These functional relationships represent the concomitant

dependence of mobility on grain size δ, flow volume V and channel width w. Table 1 shows the features of these granular flows descending curved slopes (Fig. 1).

Granular scaling parameter ψ is the product of the reciprocal of increasing functions of the numbers of clasts that 1) the flow consists of (i.e., $V^{1/3}/\delta$) and 2) the channel width has room for (i.e., w/δ). In the dense granular regime, these numbers of clasts govern flow mobility on a rough subsurface by determining clast agitation per unit of flow mass [21,22]. Clast agitation that dissipates energy is generated in contact with the rough subsurface and penetrates less inside the flow (i.e., the energy dissipation per unit of flow mass decreases), the larger the total number $\mathcal{N}$ of clasts in the flow [23,31]. Mobility becomes larger, since $\mathcal{N}$ increases, when V increases or δ decreases (all else being equal, ground roughness included). For the effect of ground roughness see refs. [21,22,32]. This δ effect is also observed in laboratory experiments [33] and other simulations [34–36]. Importantly, an increase of shear rate causes an increase of clast agitation. Indeed, in both unsteady [37] and steady [38–40] flows, frictional resistance grows with shear rate. Thus, mechanical [10] and acoustic [41] fluidizations cannot extend mobility [42–44].

In the DEM simulations, flows of the dense granular regime (i.e., with clasts relatively large in number and small in size) have their ψ versus μ_A and μ_H data points that are best-fitted by linear functional relationships with relatively large values of the coefficient of determination R^2 (Figs. 2a, b). Instead, flows consisting of only a much smaller number of coarser clasts belong to a disperse granular regime and do not fall onto those straight lines because of a mobility larger than that predicted by the lines for the ψ values of these flows (Figs. 2a, b). In this disperse regime, mobility is larger because of saltation. Fragment saltation (observed also in laboratory [45] and field measurements [46]) is concomitant with a decrease of the solid volume fraction [30] from the flow interior outwards. Saltation dissipates less energy because of far fewer solid interactions per unit of travel distance.

250

251 **Number of clasts and mobility in nature**

252

253 Here, for the concepts illustrated above to be validated in much bigger flows in nature, I use values
254 from ref. [47] of l_A, h_A, l_H, h_H, δ and V of nine rock avalanches (Table 2, with abbreviations) so that
255 an analysis of their mobility can be carried out. Their δ is the envelope middle value (at 50% passing)
256 of grain size distributions from deposit photographic measurements [47]. These field data enable the
257 calculation of: $\psi' = \delta^3/V$ (i.e., an increasing function of $1/\mathcal{N}$), μ_H and μ_A (Figs. 2c, d). Since these
258 flows are unchanneled (except rock avalanche CH, but mobility scatter of laterally confined flows
259 and that of laterally unconfined flows overlap [48]), ψ' does not contain w. The mobility range of
260 these avalanches is broad and it includes that of the computational flows (Fig. 2).

261

262 Importantly, both simulation and field data sets in Fig. 2 consist of the same typological subsets:
263 a group of flows (whose clasts are relatively larger in number and finer in size) that are best-fitted by
264 straight lines with relatively large values of R^2, and a group of flows (consisting of only fewer much
265 coarser clasts) that are not fitted by those same lines. Specifically, the seven rock avalanches with δ
266 ranging from 0.12 to 0.9 m have their mobility governed by the number of clasts since μ_H ($R^2 = 0.9$)
267 and μ_A ($R^2 = 0.8$) are linear functions of ψ' (Figs. 2c, d). Instead, the two rock avalanches with
268 coarser δ (1.6 and 4.9 m, respectively) have mobility larger than that predicted by these straight lines
269 for the ψ' values of these flows (Figs. 2c, d). Thus, in nature too, flows can have 1) a dense regime
270 behavior where the linear relationship holds (for $V/\delta^3 \geq 4.81 \times 10^6$ in Table 2) or 2) a disperse
271 regime behavior (for $V/\delta^3 \leq 3.17 \times 10^6$ in Table 2). For example, as pointed out by ref. [47], rock
272 avalanche JCN, despite a smaller volume, is more mobile than nearby rock avalanche JCS with
273 identical lithology (Fig. 2). This is explained here, in the dense regime, by the JCN larger number of
274 clasts (Table 2). Likewise, rock avalanche QE with a larger volume but fewer clasts is less mobile
275 than rock avalanche FR (Fig. 2 and Table 2). The minimum number of clasts of the dense regime

appears higher in natural avalanches than in computational flows (Tables 1 and 2) because bumpier grounds in nature require more clasts to reduce clast agitation.

Thus, $\mathcal{N}$ is a key factor governing also the mobility of volumes much bigger than those of refs. [21,22]. Although $\mathcal{N}$ of flows in nature is unknowable, its reciprocal has ψ or ψ' as proxies since they are increasing functions of $1/\mathcal{N}$. Figures 2c, d indicates that, in ψ', a single medium δ value suffices for estimating mobility (even if grain size distributions of natural avalanches are very wide [2,6]). This medium value approximates the average size of those clasts whose inelastic and frictional interactions dissipate energy in the flow interior [23,26,37,49–53] where clast motion is revealed when vertical segregation [2–4,6,44,47,54–56] appears. With "flow interior", I mean flow base and upward. Consistently, flow monodispersity does not prevent this mobility dependence on $\mathcal{N}$ from occurring (Fig. 2a, b). Figures 2c, d are important because they show that there is geologic evidence that it is the number of clasts, rather than the flow volume, that governs rock avalanche mobility in nature. This is critical for risk assessment of rock avalanches in populated areas.

Energy apportionment and dissipation in numerical simulations

In this paper, the mobility behaviors shared by simulations and nature in Fig. 2 are explained by a new energy dissipation analysis that can only be carried out by using simulation data because necessary field measurements are currently unavailable. The dissipation mechanisms are illustrated by comparing potential and kinetic energies with the work done by the non-conservative forces during all flow history to solve the mobility conundrum that μ_A and μ_H reveal but do not explain. To understand V and δ effects on mobility in terms of energy apportionment, I contrast: 1) two computational flows differing only in volume (the larger V has more clasts because δ is identical) and 2) three computational flows differing only in grain size (the finer the δ, the larger the number of clasts because V is identical).

Energy apportionment and dissipation as flow volume changes

When contrasting the two flows differing only in volume (simulations O and Q, Table 1), $\widehat{W}_i^{NC}$ of the larger-volume flow (i.e., the work done by its non-conservative forces per unit of potential energy drop to reach position ℓ_i) becomes smaller than that of the smaller-volume flow after $\ell_i/\ell_{max} = \sim 0.19$ (Fig. 3a). That is, after the deformation of the initial gravitational collapse (i.e., after the last curve intersection), the larger-volume flow dissipates less energy per unit of potential energy drop to arrive at all locations reached by the smaller-volume flow. Indeed, at the end, the center of mass of the larger-volume flow travels more (Fig. 3a).

This larger mobility is due to T_j^{ω} (the downslope translational kinetic energy per unit of work done by the non-conservative forces in a unit of travel distance) that, in almost all travel history periods Φ_j, is larger in the larger-volume flow than in the smaller-volume flow (Fig. 3b). This larger translational energy is possible because less energy is diverted into clast agitational and rotational motions inside the flow (base and upward). Surely, R_j^M(the clast rotational kinetic energy per unit of flow mass) is (in almost all periods Φ_j) much smaller in the larger-volume flow than in the smaller-volume flow (Fig. 3c). Since more intergranular space facilitates freer rotations of more clasts, the larger R_j^M in the smaller-volume flow agrees with a larger proportion of its mass being more dilated. This is due to a larger inward propagation of clast agitation (with resulting larger energy dissipation) in flows with fewer fragments [21,22]. Indeed, Λ_i (the reciprocal of an increasing function of clast agitation) of the larger-volume flow has, after the initial gravitational collapse, values larger than those of the smaller-volume flow (Fig. 4a). Both flows fall onto dense regime straight lines (Figs. 2a, b).

Energy apportionment and dissipation as grain size changes

When contrasting the three flows differing only in grain size, $\widehat{W}_i^{NC}$ of the finest-grain-size flow (simulation O, Table 1) becomes smaller than that of the two coarser-grain-size flows after $\ell_i/\ell_{max} = \sim 0.09$ (Fig. 5a). That is, after the initial gravitational collapse, the finest-grain-size flow dissipates the least energy per unit of potential energy drop to arrive at all locations reached by the coarser-grain-size flows. At the end, the center of mass of the finest-grain-size flow travels more (Fig. 5a), because (in almost all periods Φ_j) its T_j^{ω} is the largest (Fig. 5b) since more energy is allocated to downslope movement and less to clast agitational and rotational motions inside the flow (base and upward). Indeed, Λ_i of the finest-grain-size flow (after the initial gravitational collapse) is the largest (Fig. 4b), while its R_j^M (in virtually all periods Φ_j) is the smallest (Fig. 5c). This finest-grain-size flow belongs to the dense regime (Figs. 2a, b).

For the majority of their travel distance, the behaviors of these three flows agree with the concept that, in the dense regime, the coarser the grain size (all else being equal), the larger the energy dissipation because of a larger agitation per unit of flow mass in flows that, since with fewer clasts, are more dilated [21,22]. Indeed, in $\sim 0.1 < \ell_i/\ell_{max} < \sim 0.72$, the coarser the grain size, the smaller the Λ_i (Fig. 4b) and the larger the $\widehat{W}_i^{NC}$ (Fig. 5a). Moreover, in most periods Φ_j, the coarser the grain size, the smaller the T_j^{ω} (Fig. 5b) and the larger the R_j^M (Fig. 5c). Instead, in $\ell_i/\ell_{max} > \sim 0.72$, $\widehat{W}_i^{NC}$ of the coarsest-grain-size flow (simulation M, Table 1) acquires values between those of the intermediate-grain-size and finest-grain-size flows (Fig. 5a). This final mobility increase of the coarsest-grain-size flow is caused by the larger proportion of saltating mass in flows with fewer clasts [21,22]. More saltation appears in more dilated flows which is where more clasts can rotate more freely as confirmed by the much larger R_j^M of the coarsest-grain-size flow (Fig. 5c). Simulation animations prove saltation occurrence [21,22]. Thus, at the end, the coarsest-grain-size flow develops

352 a final disperse regime mobility (Figs. 2a, b). Regarding the intermediate-grain-size flow (simulation
353 N, Table 1), intermediate R_j^M and Λ_i values (during most of the travel) indicate an intermediate degree
354 of dilation: indeed, only its fronts develop a final disperse regime behavior (Fig. 2a), whereas the
355 regime behavior of its center of mass stays the dense one (Fig. 2b).
356
357 **Energy apportionment and dissipation in nature**
358
359 The energy apportionment and dissipation mechanisms in these DEM simulations are identical to
360 those in nature because of the same relationships between mobility (an energy dissipation metric) and
361 the number of clasts in the flows (Fig. 2). Indeed, in both simulations (Figs. 2a, b) and nature (Figs.
362 2c, d), the flows belong to the same dense or disperse regimes according to the same dependence of
363 mobility on the number of clasts. Therefore, also in the dense regime of rock avalanches in nature,
364 the Heim's positive correlation between volume and mobility [8,9] is caused by mechanisms intrinsic
365 to the physics of larger volumes which (as long as they have the larger number of clasts) allocate
366 more kinetic energy (per unit of dissipated energy) to downslope translational motion. This is possible
367 because dense larger-volume flows (when with the larger number of clasts) dissipate less energy (per
368 unit of potential energy drop) and they divert less energy into clast agitational and rotational motions
369 (per unit of flow mass). These mechanisms are an intrinsic feature of dense larger-volume flows
370 because they are caused by the characteristic dynamic interactions of the clasts at the base and inside
371 these flows. The energy apportionment mechanism is thus as important as the actual energy
372 dissipation in determining mobility because the kinetic energy of clasts in directions different from
373 the downslope direction and the energy allocated to clast agitational and rotational motions do not
374 increase the mobility of dense rock avalanches.
375
376 Dense larger-volume flows are more mobile as long as they have the larger number of clasts
377 because (as both simulation results and field evidence have demonstrated) it is the number of clasts,

rather than the flow volume, that governs the avalanche mobility. Indeed, there exist smaller-volume rock avalanches in nature that are more mobile because they have the larger number of clasts (as an example compare mobility and features of rock avalanches JCN and JCS in Fig. 2 and Table 2). These energy apportionment and dissipation mechanisms apply to rock avalanches when travelling after (and irrespective of) the energy dissipation of the initial slope collapse. Indeed, in Fig. 3a, despite larger values during collapse (i.e., before last curve intersection), the curve of work $\widehat{W}_i^{NC}$ of the larger-volume flow (done by its non-conservative forces per unit of potential energy drop) acquires smaller values during flow motion. The energy dissipation of the initial slope collapse needs to be much larger (the values of $\widehat{W}_i^{NC}$ are the result of a summation) to compensate for the smaller energy dissipation during motion of the larger-volume flow and neutralize its final larger mobility. Since the energy apportionment and dissipation mechanisms are governed by the number of clasts, finer-grain-size avalanches of the dense regime apportion and dissipate energy as the larger-volume avalanches do (compare Fig. 3 with Fig. 5 and Fig. 4a with Fig. 4b) because both with the larger numbers of clasts. However, in nature too, clast saltation sometimes makes a coarser-clast flow (with a smaller number of clasts) of the disperse regime more mobile than a finer-clast flow of the dense regime (as an example compare mobility and features of rock avalanches CL and AR in Fig. 2 and Table 2). The discernment of the regime the rock avalanche belongs to is thus critical to understand its mobility behavior. By considering both simulation and field data (Tables 1 and 2), it is possible to conclude that the above-mentioned energy apportionment and dissipation mechanisms of dense rock avalanches affect mobility of volumes ranging from significantly less than 0.5 million m^3 (at least from 4000–14500 m^3, if not less) to many million m^3.

Conclusions

Field data show that rock avalanches in nature belong to the same dense or disperse regimes of the flows simulated by means of the Discrete Element Method. It is therefore concluded that rock

avalanches in nature and DEM computational flows share also the same energy apportionment and dissipation mechanisms. An analysis of these mechanisms is needed to explain why dense flows of angular rock fragments with larger volumes (all else being equal) are more mobile. This larger mobility is revealed (but not explained) by parameters of the form $\mu = h/l$ (where h is a vertical drop and l is a horizontal displacement relevant for either the center of mass or the flow front). The energy analysis carried out here consists of the calculation of the energy apportioned among its different forms (including, but not limited to, that dissipated by the non-conservative forces) during the entire flow history. This analysis shows that the generation of more translational kinetic energy (per unit of dissipated energy) is an intrinsic property of dense larger-volume flows because it is caused by the characteristic dynamic interactions of the clasts at the base and inside these flows. This larger mobility is the result of the fact that dense larger-volume flows dissipate less energy (per unit of potential energy drop) and they divert less energy into clast agitational and rotational motions (per unit of flow mass). Dense larger-volume flows are, however, more mobile only when they have the larger number of clasts. Indeed, it is the number of clasts, rather than the flow volume, that governs mobility. This is confirmed by the fact that dense finer-grain-size flows (since with the larger number of clasts when all else is equal) are also more mobile. However, because of clast saltation, flows consisting of only fewer coarser clasts of a disperse regime can sometimes be more mobile than finer-grain-size flows of the dense regime. Thus, the true regime needs to be recognized for the mobility behavior of the rock avalanche to be correctly predicted.

References

1. Hungr, O., Leroueil, S. & Picarelli, L. The Varnes classification of landslide types, an update. *Landslides* **11**, 167–194 (2014).
2. Cruden, D.M. & Hungr, O. The debris of the Frank Slide and theories of rockslide-avalanche mobility. *Can. J. Earth Sci.* **23**, 425–432 (1986).

3. Hewitt, K. Catastrophic landslide deposits in the Karakoram Himalaya. *Science* **242**, 64–67 (1988).

4. Evans, S.G., Hungr, O. & Enegren, E.G. The Avalanche Lake rock avalanche, Mackenzie Mountains, Northwest Territories, Canada: description, dating and dynamics. *Can. Geotech. J.* **31**, 749–768 (1994).

5. Evans, S.G., Scarascia Mugnozza, G., Strom, A.L., Hermanns, R.L., Ischuk, A. & Vinnichenko, S. Landslides from massive rock slope failure and associated phenomena in *Landslides from massive rock slope failure* (eds. Evans, S.G., Scarascia Mugnozza, G., Strom, A. & Hermanns, R.L.) 3–52 (Springer, 2006).

6. Crosta, G.B., Frattini, P. & Fusi, N. Fragmentation in the Val Pola rock avalanche, Italian Alps. *J. Geophys. Res.* **112**, F01006 (2007).

7. Griswold, J.P. & Iverson, R.M. Mobility statistics and automated hazard mapping for debris flows and rock avalanches. *US Geological Survey Scientific Investigations Report* 2007-5276 (2008).

8. Heim, A. Bergsturz und Menschenleben (Fretz und Wasmuth Verlag, 1932).

9. Scheidegger, A.E. On the prediction of the reach and velocity of catastrophic landslides. *Rock Mech.* **5**, 231–236 (1973).

10. Davies, T.R. Spreading of rock avalanche debris by mechanical fluidization. *Rock Mech.* **15**, 9–24 (1982).

11. Legros, F. The mobility of long-runout landslides. *Eng. Geol.* **63**, 301–331 (2002).

12. Staron, L. & Lajeunesse, E. Understanding how volume affects the mobility of dry debris flows. *Geophys. Res. Lett.* **36**, L12402 (2009).

13. Crosta, G.B., Frattini, P., Valbuzzi, E. & Hermanns, R.L. The Cerro Caquilluco - Cerrillos Negros giant rock avalanches (Tacna, Peru) in *Engineering geology for society and territory - volume 2* (eds. Lollino, G., Giordan, D., Crosta, G.B., Corominas, J., Azzam, R., Wasowski, J. & Sciarra, N.) 921–924 (Springer, 2015).

14. Strom, A. & Abdrakhmatov, K. Rockslides and Rock Avalanches of Central Asia: Distribution, Morphology and Internal Structure (Elsevier, 2018).

15. Mitchell, A., McDougall, S., Nolde, N., Brideau, M.A., Whittall, J. & Aaron, J.B. Rock avalanche runout prediction using stochastic analysis of a regional dataset. *Landslides* **17**, 777–792 (2020).

16. Hsü, K.J. Catastrophic debris streams (sturzstroms) generated by rockfalls. *Geol. Soc. Am. Bull.* **86**, 129–140 (1975).

17. Nicoletti, P.G. & Sorriso-Valvo, M. Geomorphic controls of the shape and mobility of rock avalanches. *Geol. Soc. Am. Bull.* **103**, 1365–1373 (1991).

18. Straub, S. Predictability of long runout landslide motion: implications from granular flow mechanics. *Geol. Rundsch.* **86**, 415–425 (1997).

19. Kilburn, C.R.J. & Sørensen, S.A. Runout lengths of sturzstroms: The control of initial conditions and of fragment dynamics. *J. Geophys. Res.* **103**, 17877–17884 (1998).

20. Corominas, J. The angle of reach as a mobility index for small and large landslides. *Can. Geotech. J.* **33**, 260–271 (1996).

21. Cagnoli, B. Stress level effect on mobility of dry granular flows of angular rock fragments. *Landslides* **18**, 3085–3099 (2021).

22. Cagnoli, B. Flow front mobility of rock avalanches as a function of flow volume, grain size, channel width, basal friction and flow scale. *Landslides* **21**, 933–947 (2024).

23. Cagnoli, B. & Romano, G.P. Effects of flow volume and grain size on mobility of dry granular flows of angular rock fragments: A functional relationship of scaling parameters. *J. Geophys. Res.* **117**, B02207 (2012a).

24. Bowman, E.T., Laue, J., Imre, B. & Springman, S.M. Experimental modelling of debris flow behaviour using a geotechnical centrifuge. *Can. Geotech. J.* **47**, 742–762 (2010).

25. Cundall, P.A. & Strack, O.D.L. A discrete numerical model for granular assemblies. *Géotechnique* **29**, 47–65 (1979).

26. Cagnoli, B. & Piersanti, A. Grain size and flow volume effects on granular flow mobility in numerical simulations: 3-D discrete element modeling of flows of angular rock fragments. *J. Geophys. Res. Solid Earth* **120**, 2350–2366 (2015).

27. Becker, G.F. A feature of Mayon Volcano. *Proc. Wash. Acad. Sci.* **7**, 277–282 (1905).

28. Cagnoli, B. & Piersanti, A. Combined effects of grain size, flow volume and channel width on geophysical flow mobility: three-dimensional discrete element modeling of dry and dense flows of angular rock fragments. *Solid Earth* **8**, 177–188 (2017).

29. Iverson, R.M. Scaling and design of landslide and debris-flow experiments. *Geomorphology* **244**, 9–20 (2015).

30. Zhou, G.G.D. & Sun, Q.C. Three-dimensional numerical study on flow regimes of dry granular flows by DEM. *Powder Technol.* **239**, 115–127 (2013).

31. Cagnoli, B. & Romano, G.P. Granular pressure at the base of dry flows of angular rock fragments as a function of grain size and flow volume: A relationship from laboratory experiments. *J. Geophys. Res.* **117**, B10202 (2012b).

32. Sosio, R., Crosta, G.B., Chen, J.H. & Hungr, O. Modelling rock avalanche propagation onto glaciers. *Quat. Sci. Rev.* **47**, 23–40 (2012).

33. Cagnoli, B. & Romano, G.P. Effect of grain size on mobility of dry granular flows of angular rock fragments: An experimental determination. *J. Volcanol. Geotherm. Res.* **193**, 18–24 (2010).

34. Mollon, G., Richefeu, V., Villard, P. & Daudon, D. Discrete modelling of rock avalanches: sensitivity to block and slope geometries. *Granular Matter* **17**, 645–666 (2015).

35. Lai, Z., Vallejo, L.E., Zhou, W., Ma, G., Espitia, J.M., Caicedo, B. & Chang, X. Collapse of granular columns with fractal particle size distribution: Implications for understanding the role of small particles in granular flows. *Geophys. Res. Lett.* **44**, 12181–12189 (2017).

36. Johnson, B.C. & Campbell, C.S. Drop height and volume control the mobility of long-runout landslides on the Earth and Mars. *Geophys. Res. Lett.* **44**, 12091–12097 (2017).

37. Campbell, C.S., Cleary, P.W. & Hopkins, M. Large-scale landslide simulations: Global deformation, velocities and basal friction. *J. Geophys. Res.* **100**, 8267–8283 (1995).

38. Bagnold, R.A. Experiments on a gravity-free dispersion of large solid spheres in a Newtonian fluid under shear. *Proc. R. Soc. Lond. A* **225**, 49–63 (1954).

508 39. G.D.R. Mi.Di. On dense granular flows. *Eur. Phys. J. E* **14**, 341–365 (2004).
509 40. Jop, P., Forterre, Y. & Pouliquen, O. A constitutive law for dense granular flows. *Nature* **441**,
510 727–730 (2006).
511 41. Melosh, H.J. Acoustic fluidization: a new geologic process? *J. Geophys. Res.* **84**, 7513–7520
512 (1979).
513 42. Hungr, O. & Morgenstern, N.R. Experiments on the flow behaviour of granular materials at high
514 velocity in an open channel. *Géotechnique* **34**, 405–413 (1984a).
515 43. Hungr, O. & Morgenstern, N.R. High velocity ring shear tests on sand. *Géotechnique* **34**, 415–
516 421 (1984b).
517 44. Hungr, O. Rock avalanche occurrence, process and modelling in *Landslides from massive rock*
518 *slope failure* (eds. Evans, S.G., Scarascia Mugnozza, G., Strom, A. & Hermanns, R.L.) 243–266
519 (Springer, 2006).
520 45. Bryant, S.K., Take, W.A. & Bowman, E.T. Observations of grain-scale interactions and
521 simulation of dry granular flows in a large-scale flume. *Can. Geotech. J.* **52**, 638–655 (2015).
522 46. Schaer, M. & Issler, D. Particle densities, velocities and size distributions in large avalanches
523 from impact-sensor measurements. *Ann. Glaciol.* **32**, 321–327 (2001).
524 47. Locat, P., Couture, R., Leroueil, S., Locat, J. & Jaboyedoff, M. Fragmentation energy in rock
525 avalanches. *Can. Geotech. J.* **43**, 830–851 (2006).
526 48. Strom, A., Li, L. & Lan, H. Rock avalanche mobility: optimal characterization and the effects of
527 confinement. *Landslides* **16**, 1437–1452 (2019).
528 49. Savage, S.B. The mechanics of rapid granular flows. *Adv. Appl. Mech.* **24**, 289–366 (1984).
529 50. Savage, S.B. Streaming motions in a bed of vibrationally fluidized dry granular material. *J. Fluid*
530 *Mech.* **194**, 457–478 (1988).
531 51. Legros, F., Cantagrel, J.M. & Devouard, B. Pseudotachylyte (frictionite) at the base of the
532 Arequipa volcanic landslide deposit (Peru): Implications for emplacement mechanisms. *J. Geol.*
533 **108**, 601–611 (2000).

52. Bartelt, P., Buser, O. & Platzer, K. Fluctuation-dissipation relations for granular snow avalanches. *J. Glaciol.* **52**, 631–643 (2006).

53. Manzella, I. & Labiouse, V. Empirical and analytical analyses of laboratory granular flows to investigate rock avalanches propagation. *Landslides* **10**, 23–36 (2013).

54. Strom, A. Morphology and internal structure of rockslides and rock avalanches: grounds and constraints for their modelling in *Landslides from massive rock slope failure* (eds. Evans, S.G., Scarascia Mugnozza, G., Strom, A. & Hermanns, R.L.) 305–326 (Springer, 2006).

55. Mitani, N.K., Matuttis, H.G. & Kadono, T. Density and size segregation in deposits of pyroclastic flow. *Geophys. Res. Lett.* **31**, L15606 (2004).

56. Cagnoli, B. & Romano, G.P. Vertical segregations in flows of angular rock fragments: Experimental simulations of the agitation gradient within dense geophysical flows. *J. Volcanol. Geotherm. Res.* **265**, 52–59 (2013).

Statements and Declarations

Author contribution This is a one author paper.

Funding This study was funded by Istituto Nazionale di Geofisica e Vulcanologia.

Data availability Data will be made available on request.

Code availability Software EDEM version 2021.2 used to carry out the simulations is owned by Siemens and it is accessible under license.

Acknowledgements A CINECA award under the ISCRA initiative is warmly thanked for the technical assistance and the high-performance computing resources that have been provided.

Competing interests The author declares no competing interests.

Simulations	δ (m)	V (m^3)	V/δ^3	w (m)	w/δ
O	0.5	~ 9852	78815	6	12
Q	0.5	~ 4080	32638	6	12
P	1	~ 14533	14533	26	26
N	1	~ 9852	9852	6	6
M	2	~ 9852	1231	6	3

Table 1. Computational flows of angular rock clasts. δ, V and w values from refs. [21,22]. V/δ^3 is the number of clasts.

Rock avalanches	abbreviation	δ (m)	V (m^3)	V/δ^3
Frank Slide	FR	0.25	30×10^6	1.92×10^9
Queen Elizabeth	QE	0.83	45×10^6	7.87×10^7
Jonas Creek North	JCN	0.40	2.4×10^6	3.75×10^7
Jonas Creek South	JCS	0.90	4.9×10^6	6.72×10^6
La Madeleine	LM	0.12	90×10^6	5.21×10^{10}
Charmonétier	CH	0.30	0.13×10^6	4.81×10^6
Arvel	AR	0.50	0.61×10^6	4.88×10^6
Slide Mountain	SM	1.60	13×10^6	3.17×10^6
Claps de Luc	CL	4.90	2×10^6	1.70×10^4

Table 2. Natural rock avalanches. δ and V values from ref. [47]. V/δ^3 is an increasing function of the number of clasts.

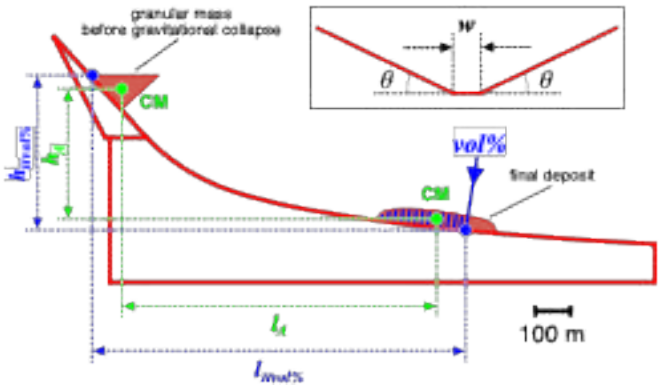


Fig. 1. Longitudinal and transversal profiles of the channels in the numerical simulations. The Heim's coefficient is computed for each volume percent ($vol\%$) as the ratio of the vertical ($h_{Hvol\%}$) to the horizontal ($l_{Hvol\%}$) distances between the rear top end of the granular mass before release and the front of that $vol\%$ of deposit. CM stands for center of mass whose inverse of mobility is the ratio of its vertical (h_A) to horizontal (l_A) displacements. The inset shows the trapezoidal cross-section in the transversal direction of both straight and curved portions of the channels.

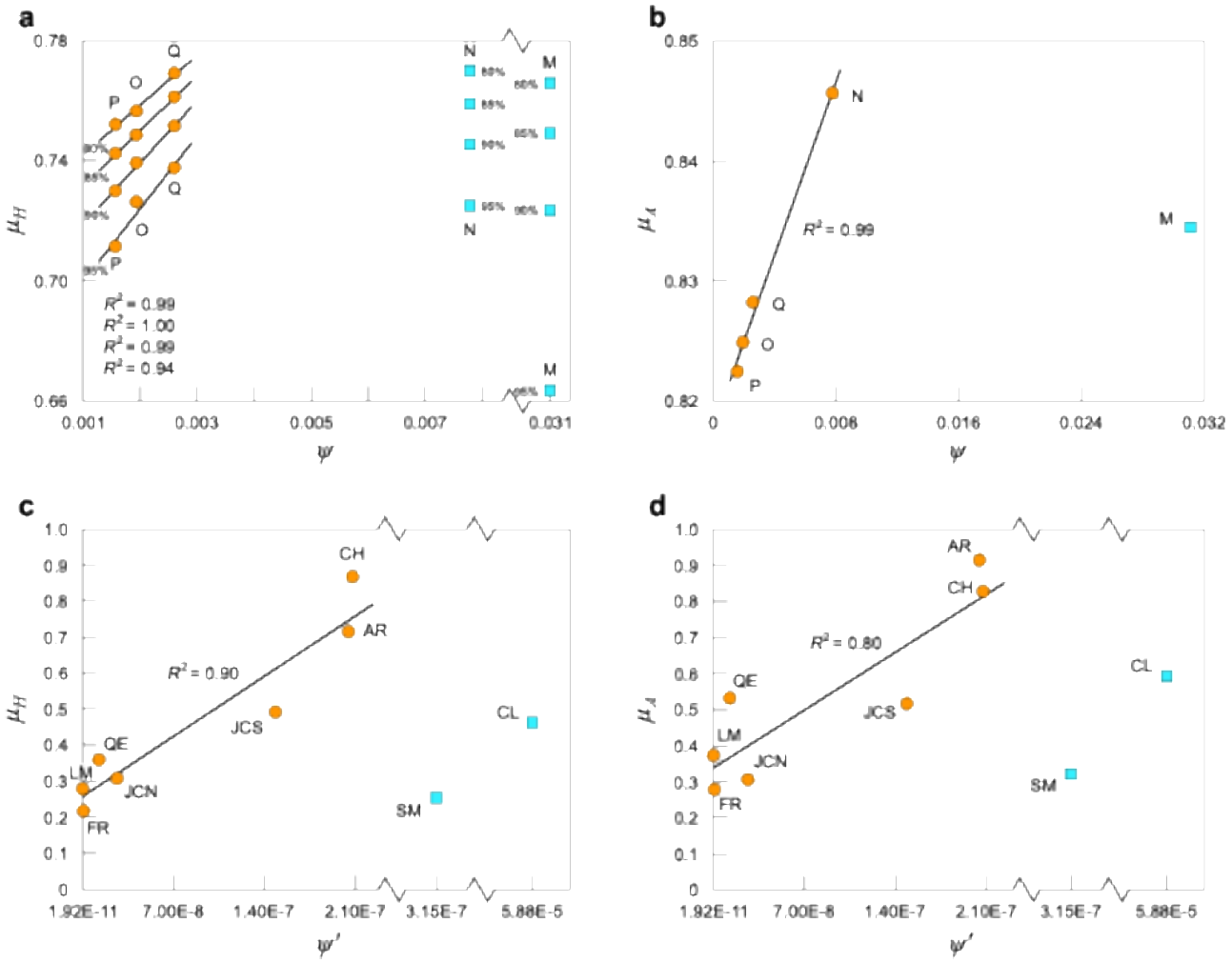


Fig. 2. Mobility of computational flows and natural rock avalanches. This figure shows the dense (orange circles) and the disperse (turquoise squares) granular regimes. **a** Reciprocal of computational mobility of the fronts of different volume percentages ($vol\%$). Fronts of simulations P, O and Q are best-fitted by straight lines. Those of simulations M and N are not. The R^2 values are in the same vertical order of the straight lines they belong to. **b** Reciprocal of computational mobility of the center of mass. Only that of simulation M is not best-fitted by the straight line. **c** Reciprocal of field mobility of the fronts of rock avalanches in nature. Fronts of avalanches FR, LM, QE, JCN, JCS, CH and AR are best-fitted by a straight line. Those of avalanches SM and CL are not. **d** Reciprocal of field mobility of the center of mass of rock avalanches in nature. Centers of mass of avalanches FR, LM, QE, JCN, JCS, CH and AR are best-fitted by a straight line. Those of avalanches SM and CL are not.

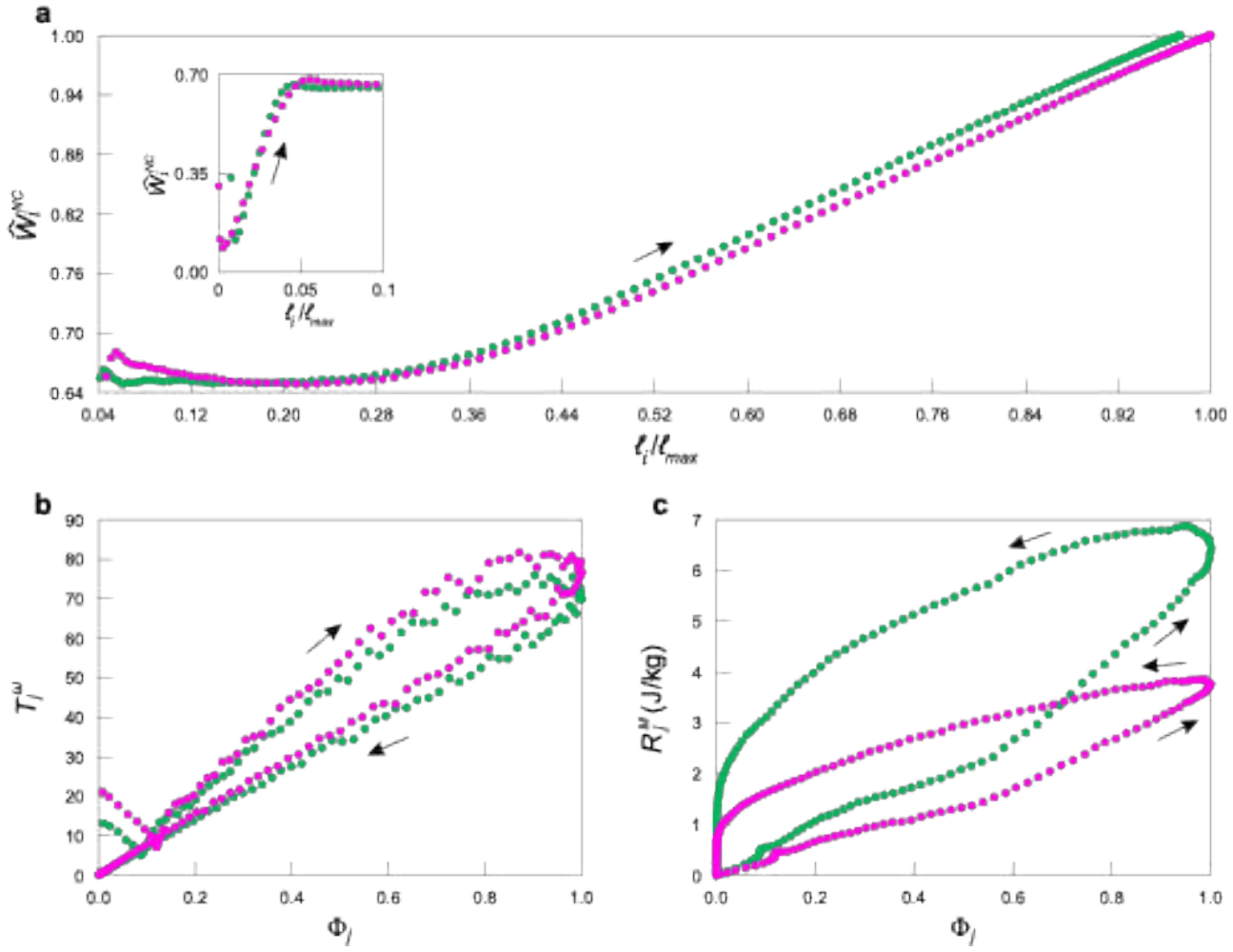


Fig. 3. Energy apportionment and dissipation in computational flows differing only in volume. The flows are those of simulations O (larger V, magenta circles) and Q (smaller V, green circles). Direction of time shown by arrows. **a** Work done by non-conservative forces (per unit of potential energy drop) for the center of mass to travel distances ℓ_i normalized by the longer distance ℓ_{max} which is the final one of the larger-volume flow. Inset includes initial gravitational collapses. **b** Downslope translational kinetic energy (per unit of work done by non-conservative forces in a unit of travel distance) versus travel history period Φ_j. After release, each flow accelerates from left to right on upper path of its data loop and then it decelerates on lower path. **c** Clast rotational kinetic energy (per unit of flow mass) versus Φ_j. After release, each flow accelerates from left to right on lower path of its data loop and then it decelerates on upper path.

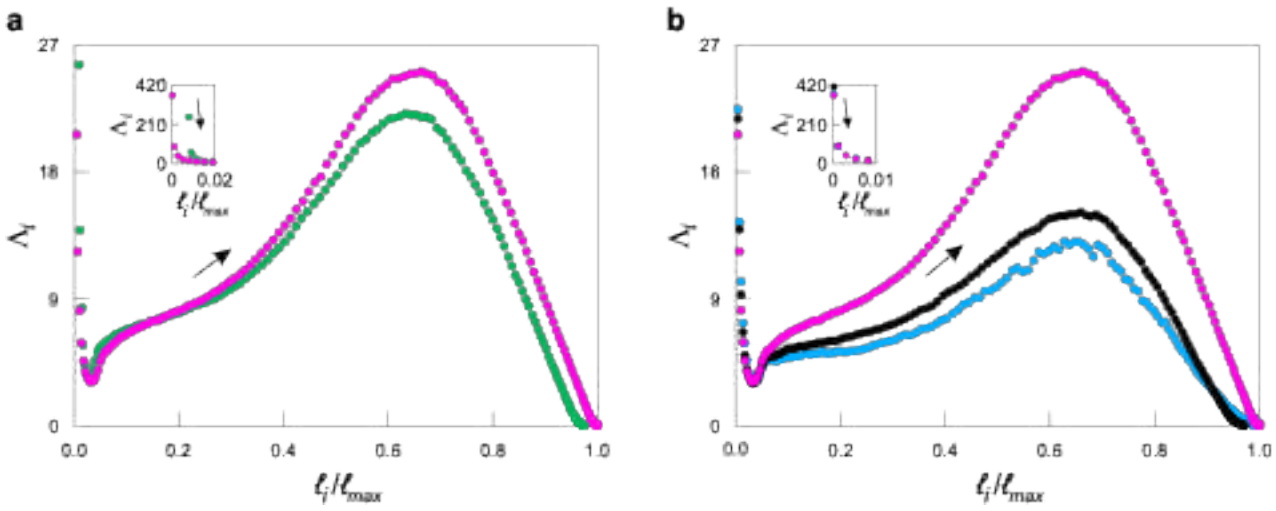


Fig. 4. Energy apportionment concerning clast agitation in computational flows differing only in volume or grain size. Λ_i is the reciprocal of an increasing function of clast agitation. Insets display beginning of initial gravitational collapses. Direction of time shown by arrows. **a** Flows are those of simulations O (larger V, magenta circles) and Q (smaller V, green circles). Travel distances ℓ_i of the center of mass are normalized by longer distance ℓ_{max} which is the final one of the larger-volume flow. **b** Flows are those of simulations O (finest δ, magenta circles), N (intermediate δ, black circles) and M (coarsest δ, blue circles). Travel distances ℓ_i of the center of mass are normalized by longest distance ℓ_{max} which is the final one of the finest-grain-size flow.

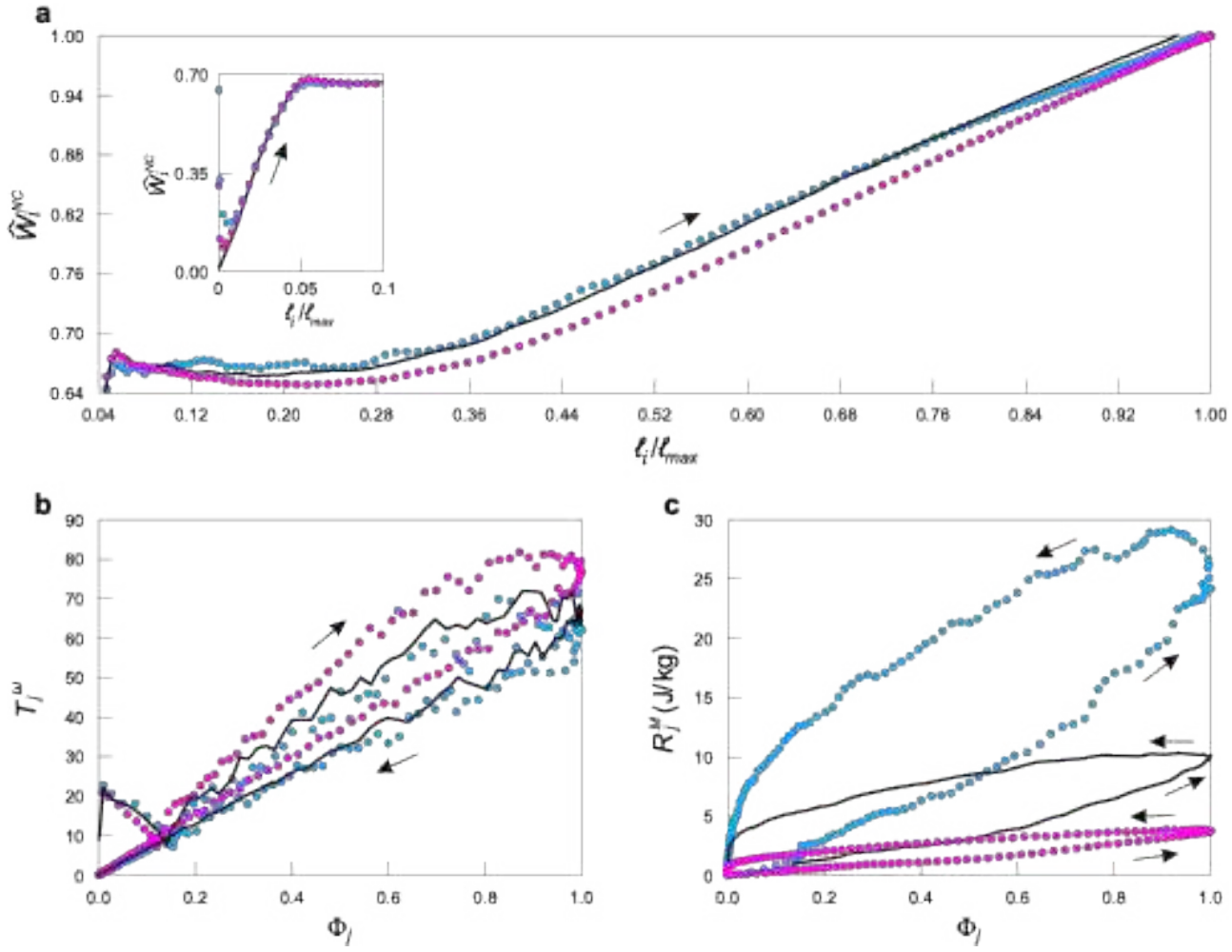


Fig. 5. Energy apportionment and dissipation in computational flows differing only in grain size. The flows are those of simulations O (finest δ, magenta circles), N (intermediate δ, black lines) and M (coarsest δ, blue circles). Direction of time shown by arrows. **a** Work done by non-conservative forces (per unit of potential energy drop) for the center of mass to travel distances ℓ_i normalized by longest distance ℓ_{max} which is the final one of the finest-grain-size flow. Inset includes initial gravitational collapses. **b** Downslope translational kinetic energy (per unit of work done by non-conservative forces in a unit of travel distance) versus travel history period Φ_j. After release, each flow accelerates from left to right on upper path of its data loop and then it decelerates on lower path. **c** Clast rotational kinetic energy (per unit of flow mass) versus Φ_j. After release, each flow accelerates from left to right on lower path of its data loop and then it decelerates on upper path.